Kovove Mater. 64 2026 13–25
DOI: 10.31577/km.2026.1.13

High temperature friction and wear of spark plasma sintered Ti-Cu matrix friction composites with additions of machining metal wastes and reinforced with graphene nanoplatelets and ceramic particles

Mária Podobová[1]*, Viktor Puchý[1], Róbert Džunda[1], František Kromka[1], Ondrej Milkovič[1,2], Michal Besterci[1]

[1] *Institute of Materials Research, Slovak Academy of Sciences, Watsonova 47, 040 01 Košice, Slovak Republic*
[2] *Institute of Experimental Physics, Slovak Academy of Sciences, Watsonova 47, 04001 Košice, Slovak Republic*

Received 17 December 2025, received in revised form 21 January 2026, accepted 22 January 2026

Abstract

This study focuses on the wear behaviour of Ti-Cu-based friction composites during tribological testing at 350 ℃ under a load of 5 N and a sliding distance of 500 m. Composites were fabricated using a planetary ball mill and Spark Plasma Sintering (SPS). A mixture based on Ti and Cu is supplemented with waste-metal components (stainless steel, CuZn, and MgAl), reinforced with Al_2O_3 and graphene, and also serves as a lubricant. The Coefficient of Friction (COF) was determined using a ball-on-disc technique with a 100Cr6 ball as the counterbody. Microstructure and mechanical properties were determined using a Scanning Electron Microscope (SEM), Energy-Dispersive X-ray Spectroscopy (EDS), and confocal microscopy. SEM/EDS and 3D confocal profilometry reveal that the CuZn-containing composite (TC3) forms the smoothest and most continuous Cu/Zn-oxide-carbon glaze-like film, which minimizes abrasive wear and results in the mildest polishing of the counterbody. It combines the highest but most stable COF (~ 0.75) with a ~ 25 % lower ball penetration depth than TC2 with MgAl.

K e y w o r d s: Ti-Cu matrix, friction composites, hot tribological test, friction, wear, metal wastes

1. Introduction

Friction materials used in braking systems must maintain a stable coefficient of friction and adequate wear resistance over a wide temperature range, often up to 300–400 ℃ in service. Modern brake pads are typically multi-ingredient composites containing fibres, fillers, lubricants, and friction modifiers, and are classified as semi-metallic, non-asbestos organic (NAO), low-metallic NAO, or ceramic [1–3]. While NAO and ceramic formulations offer low noise and reduced dust, semi-metallic and low-metallic materials provide superior load-bearing capacity and heat dissipation, which are essential under severe braking conditions [1, 3]. The ongoing challenge is to combine the thermal stability and braking efficiency of metal-based pads with the low noise and environmental benefits of NAO/ceramic formulations in a single material concept [1, 3]. Metal-matrix friction composites based on Cu, Fe, or Ti have therefore attracted increasing attention as candidates for high-temperature braking applications [2, 4–6]. Lightweight titanium and copper alloys offer favourable strength-to-weight ratios and thermal conductivity, but their intrinsic friction and wear behaviour are often insufficient at high loads and elevated temperatures [5, 7–9]. To overcome these limitations, hard ceramic particles such as Al_2O_3, ZTA, or carbides are introduced to stabilise the contact, increase hardness, and tailor the tribological response [10–14]. Several studies have demonstrated that Al_2O_3-reinforced Al- and Ti-based metal-matrix composites can significantly improve hardness and re-

*Corresponding author: tel.: +421-55-792-2448; e-mail address: mpodobova@saske.sk

duce wear compared with the unreinforced alloys, with wear surfaces characterised by adhesive, delamination, and smear layers typical of oxidative sliding regimes [11–14]. In parallel, advanced processing routes such as Spark Plasma Sintering (SPS) and related powder metallurgy techniques are increasingly used to consolidate multiphase friction composites with refined microstructures and controlled porosity, including Cu- and Ti-based friction materials for high-temperature service [5, 6, 9, 13]. In addition to ceramic reinforcements, solid lubricants play a key role in controlling friction and mitigating severe wear at elevated temperatures. Carbon-based solid lubricants – including graphite, carbon nanotubes, and graphene derivatives – have been widely investigated in polymers, coatings, and metal-matrix composites because they can form low-shear tribofilms and reduce counterbody damage [15–19]. Graphene and graphene nanoplatelets (GNPs), in particular, are considered emerging lubricants owing to their high in-plane stiffness, thermal conductivity, and ability to generate thin, load-bearing carbon films on sliding surfaces [17–20]. Studies on GNP-reinforced Al, Ni, and Ti-based systems have shown that graphene-containing tribofilms can decrease friction, stabilise wear rates, and protect steel counterparts, especially when combined with oxide-forming metallic matrices [7, 16–19]. At higher temperatures, the interplay between tribo-oxidation and carbon-based lubrication becomes critical: compact oxide-carbon "glaze" layers can support the load while maintaining a relatively low coefficient of friction [16–20]. At the same time, there is increasing pressure to reduce the environmental footprint of friction materials by incorporating recycled or waste-derived constituents. Prior work on friction composites reinforced with natural fibres, industrial by-products, or secondary metallic powders has demonstrated that such materials can achieve competitive mechanical and tribological performance while reducing raw material consumption [4, 5, 21, 22]. In our previous studies, we proposed metal-matrix composites in which a substantial fraction of the metallic phase is derived from machining waste (Ti, Cu, and various waste-metal additives), combined with ceramic and lubricating components for brake-like applications [4, 23]. These works showed that Ti-Cu-based waste-metal composites reinforced with Al_2O_3 and GNPs can be successfully fabricated by high-energy ball milling and SPS, and that at room temperature they exhibit promising friction coefficients and wear resistance under dry sliding conditions [4, 23]. However, the service temperature of practical brake pads usually does not exceed about 400 °C, and the performance of such waste-metal-rich composites under hot tribological conditions remains far less explored [3, 4, 5, 23]. Despite the growing literature on self-lubricating metal-matrix composites and graphene-reinforced tribosystems, there is still a lack of systematic data on the high-temperature friction behaviour of Ti-Cu matrix composites in which (i) the metallic phase is largely derived from machining waste and (ii) the system is simultaneously reinforced by ceramic particles and GNPs [4, 7, 9, 16–19]. In particular, the effects of different waste-metal additions (such as stainless steel, MgAl, or CuZn) on microstructural development during SPS and on the formation and stability of oxide-carbon tribofilms at ∼ 350 °C remain unclear [4, 5, 23]. This knowledge is essential for designing sustainable friction composites that operate in the tribo-oxidative regime, with stable friction coefficients in the range 0.3–0.7 and limited wear of both the composite and the steel counterpart. Therefore, the present work investigates the friction and wear behaviour at 350 °C of three SPS-consolidated Ti-Cu-X-Al_2O_3-GNP friction composites (X = stainless steel, MgAl, and CuZn) produced from a mixture of raw and waste metallic components. Building on our earlier room-temperature study of similar materials [23], we focus here on (i) the evolution and stabilisation of the coefficient of friction and penetration depth under ball-on-disc sliding, and (ii) the correlation between SPS-induced microstructures, hot wear mechanisms, and the chemistry and morphology of oxide-carbon tribofilms formed on both the composite and the 100Cr6 steel counterbody. By linking the composition-dependent tribofilm formation to the high-temperature tribological response, we aim to identify which waste-metal addition offers the most favourable balance between sustainability and performance for high-temperature friction applications.

However, there is a lack of systematic data on the high-temperature friction behaviour of Ti-Cu matrix composites reinforced with graphene nanoplatelets and ceramic particles when the metallic phase is largely derived from machining waste. In particular, the role of different waste-metal additions (stainless steel, MgAl, and CuZn) in controlling the formation and stability of oxide–carbon tribofilms at ∼ 350 °C remains poorly understood.

2. Materials and methods

2.1. Starting materials, waste-metal feedstocks, and compositions

Three Ti-Cu-based friction composites were prepared with different waste-metal additions, denoted TC1–TC3. Titanium and copper for the matrix originated from machining operations (chips of various sizes and morphologies). The modifier additions were selected as representative waste-/secondary metallic constituents: stainless steel (SSt), MgAl alloy, and CuZn brass. MgAl and CuZn were used in the form of machining waste powders/chips, while stainless steel

Table 1. Starting materials and waste-metal additions used for the preparation of TC1–TC3 composites

Constituent	Type	Origin/initial form	Pre-processing before blending	Primary role in composite (tribological motivation)
Ti	Waste-metal	Machining waste: chips of various sizes/shapes	Pre-refining in the UFO disc mill (2 × 5 min) due to coarse structure	Thermally/chemically stable metallic skeleton; supports high-T tribo-oxidative operation
Cu	Waste-metal	Machining waste: chips	Directly blended (after the common HEBM step)	Heat conduction supports Cu-rich tribofilm/glaze formation at HT
Stainless steel (SS, SSt)	Waste-metal (waste-like feedstock)	Stainless-steel wire sponge (commercial scourer)	Pre-refining in UFO disc mill (2 × 5 min) to obtain powder-like fragments	Fe/Cr-rich oxide patches at HT (load-bearing but potentially abrasive)
MgAl	Waste-metal	Machining waste: powders/chips	Directly blended (after the common HEBM step)	Promotes Mg-Al-O oxide/spinel-type tribolayer; hardness/oxidation control
CuZn (brass)	Waste-metal	Machining waste: powders/chips	Directly blended (after the common HEBM step)	Supports compact Cu/Zn-oxide-carbon "glaze" tribofilm at HT
Al_2O_3	Raw ceramic	Powder (as received)	Directly blended (after the common HEBM step)	Load-bearing reinforcement; wear resistance
GNPs	Raw lubricant	Graphene nanoplatelets/graphene nanoparticles (as received)	Directly blended (after the common HEBM step)	Solid lubrication; carbon-rich low-shear tribofilm

was introduced as a commercially available stainless-steel wire sponge (scourer) serving as an easily accessible waste-like SSt feedstock. The ceramic reinforcement was Al_2O_3 powder, and the solid lubricant was graphene nanoplatelets (GNPs), both used as received. Table 1 includes details about the used components.

The nominal compositions of the composites were (wt.%):

TC1: 40Ti-25Cu-15SS-15Al_2O_3-5GNPs,

TC2: 40Ti-25Cu-15MgAl-15Al_2O_3-5GNPs,

TC3: 40Ti-25Cu-15CuZn-15Al_2O_3-5GNPs.

Because Ti chips and SSt wire sponge exhibit a coarse, irregular morphology, these two constituents were pre-refined before blending to obtain powder-like fragments suitable for homogeneous mixing. The pre-refining was carried out in a UFO disc mill (WAB AG, Switzerland) for 2 × 5 min.

A brief rationale for the selected constituents is as follows: Ti provides thermal/chemical stability to the metallic skeleton; Cu improves heat conduction and supports the formation of Cu-rich tribofilms; Al_2O_3 acts as a load-bearing, wear-resistant reinforcement; and GNPs serve as a solid lubricant, promoting low-shear carbon-rich tribofilms. The waste-metal modifiers were chosen to compare different tribo-oxidation/tribofilm pathways at elevated temperature: stainless steel (Fe-Cr-Ni based) is expected

to promote formation of Fe/Cr-rich oxide patches that can locally support load but may increase abrasivity; MgAl can promote formation of Mg-Al-O oxide/spinel regions with high hardness; and CuZn (brass) can facilitate formation of compact Cu/Zn-oxide-carbon glaze-like films in the tribo-oxidative regime.

2.2. Powder processing and blending

After the pre-refining step (Ti and SS), all components were combined and homogenized by high-energy ball milling (HEBM) in a planetary mill (RETSCH PM 100). Milling was performed at 250 rpm for 2 h using WC grinding balls, with a powder-to-ball mass ratio of 5 : 1.

All constituents were homogenized by high-energy ball milling (250 rpm, 2 h, WC balls, powder balls = 5 : 1) in ethanol, followed by drying (90 ℃, 8 h). Titanium chips and stainless-steel wire sponge were pre-refined in a UFO disc mill (2 × 5 min) due to their coarse initial morphology.

Ethanol was used as a milling medium. The milled suspension was subsequently dried for 8 h at 90 ℃ to obtain the final composite powder blends for sintering.

2.3. Spark plasma sintering (SPS)

Disc-shaped samples (diameter 20 mm) were consolidated by spark plasma sintering using an HP D 10SD SPS system (FCT Systeme, Frankenblick, Germany). Sintering was carried out under vacuum (∼ 5 Pa) with pulsed DC (pulse duration 15 ms, pause 3 ms). A top pyrometer monitored temperature focused into the punch hole at a distance of ∼ 4 mm from the sample. The SPS parameters were: sintering temperature 1000 ℃, heating rate 100 ℃ min^{-1}, dwell time 10 min, and applied pressure 50 MPa. The resulting disc thickness was approximately 4 mm.

2.4. High-temperature tribological testing (this work) and room-temperature reference (previous work)

High-temperature (HT) ball-on-disc tribological tests were performed in laboratory air at 350 ℃ using a CSM Instruments tribometer (CSM Instruments SA, Peseux, Switzerland). A polished 100Cr6 bearing steel ball (diameter 6 mm) was used as the counterbody. The test parameters were: normal load 5 N, sliding speed 100 mm s^{-1}, and total sliding distance 500 m. During HT tests, the coefficient of friction (COF) and penetration depth were recorded continuously by the tribometer. For each composite (TC1–TC3), at least three independent HT tests were performed under identical conditions ($n \geq 3$).

For clarity, room-temperature ball-on-disc tribotesting (friction and wear in air) was previously reported for related Ti-Cu-Al_2O_3-GNP waste-metal composites and is cited here only as background [23]; the present manuscript reports high-temperature tests at 350 ℃.

2.5. Post-test and microstructural characterization

After sintering and after the HT tribological tests, the microstructure and worn surfaces were analyzed by SEM equipped with EDS (Tescan Vega-3 LMU, Brno, Czech Republic; Bruker XFlash Detector 410-M, Billerica, MA, USA). The morphology of wear tracks and the wear mechanisms were evaluated by a confocal 3D optical profiler (PLu neox, SENSOFAR, Barcelona, Spain). Phase analysis before and after tribotesting ("no track" and "track") was performed by X-ray diffraction (Philips X'Pert Pro, Malvern Panalytical, Almelo, The Netherlands) using Cu-Kα radiation in Bragg-Brentano geometry, in the 20°–100° 2θ range with a step size of 0.03° and a counting time of 30 s per step.

3. Results and discussion

3.1. Microstructural development of SPS-consolidated Ti-Cu-X-Al_2O_3-GNP composites

The optical microstructures of composites TC1–TC3 (Figs. 1a–c) confirm the distinct multiphase morphology typical of rapid, pulse-controlled SPS sintering. All three materials exhibit sharp interfaces between the metal matrix (Ti-Cu base), dispersed Al_2O_3 ceramic particles, and segregated clusters of the modifier component (Stainless Steel, MgAl, or CuZn). The contrasting colour distribution reflects local differences in chemical composition and in the solidifying metallic phases after short-term SPS heating. Composite TC1 (Fig. 1a) shows the highest microstructural heterogeneity. The presence of stainless steel leads to a local enrichment of Fe-Cr-Ni phases, which do not dissolve homogeneously in the Ti-Cu matrix during SPS. The bright orange areas represent Cu-rich segments, and the darker, fine-grained zones are associated with the Ti matrix and high Al_2O_3 content. The sharp phase boundaries indicate fast sintering kinetics and limited diffusion of Fe-containing components. This results in local segregation of metallic phases, which can reduce mechanical homogeneity but also create hard islands with potentially higher wear resistance. The microstructure of TC2 in Fig. 1b is the most homogeneous of the three samples. The presence of MgAl alloy lowers the local melting temperature and promotes more uniform sintering, as evidenced by smaller phase con-

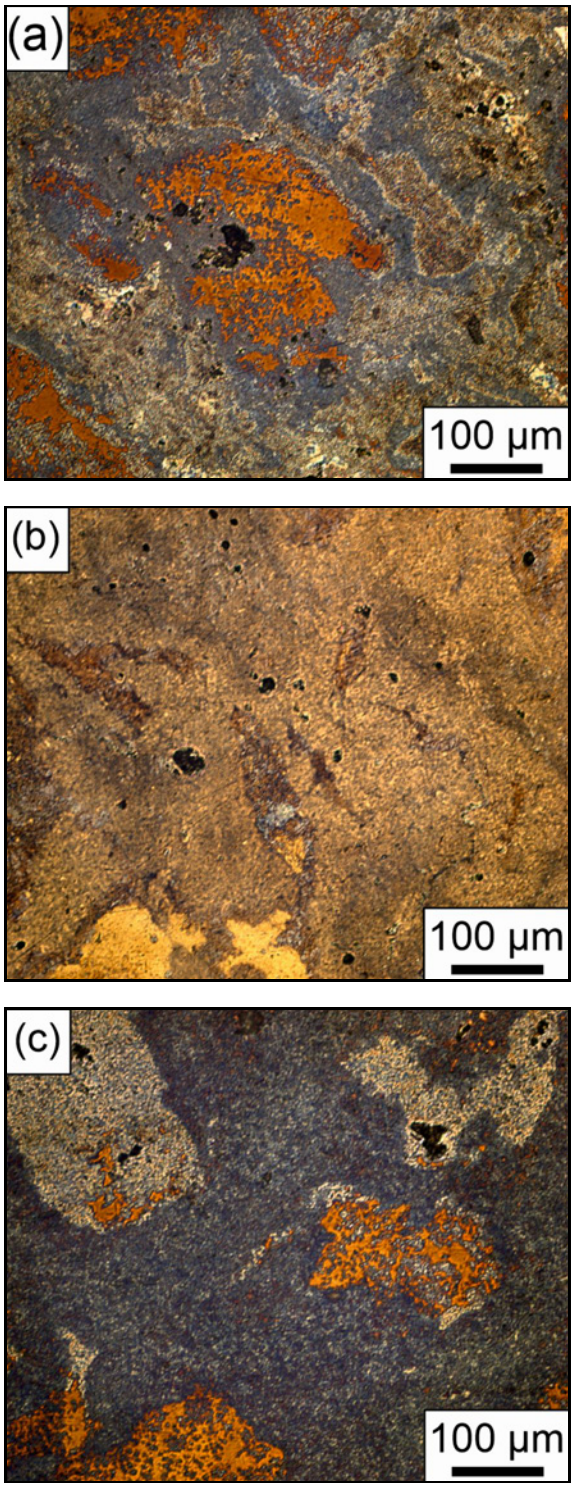

Fig. 1. OM of friction-composite samples (a) TC1, (b) TC2, and (c) TC3.

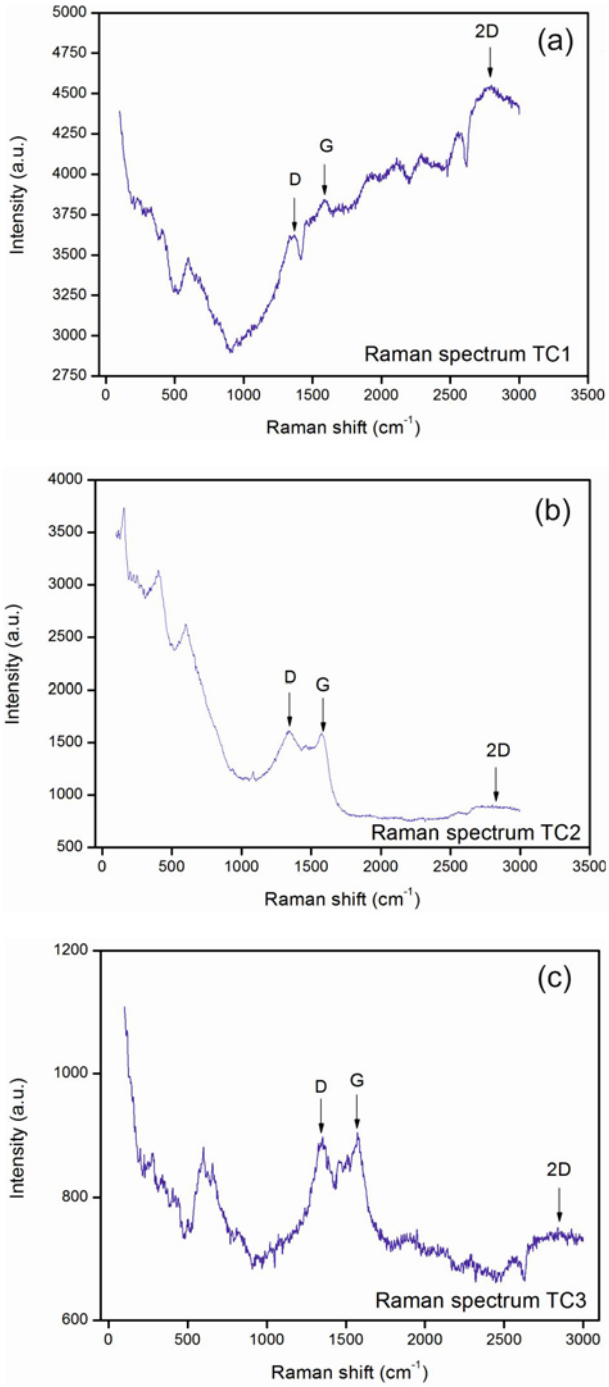

Fig. 2. Raman spectra of friction-composite samples (a) TC1, (b) TC2, and (c) TC3.

trasts. Despite the higher macro-homogeneity, scattered pores are observed, which mainly form at the metal-GNPs interface. GNPs act as diffusion barriers and can locally limit compaction, which explains the higher porosity of TC2. This effect can reduce strength but, at the same time, improve damping and tribological properties. The apparent density was calculated as the ratio of the apparent volume to the dry mass of the prepared samples. The measured values were as follows: 5.140 $\mathrm{g\,cm^{-3}}$ (TC1), 4.523 $\mathrm{g\,cm^{-3}}$ (TC2), and 4.526 $\mathrm{g\,cm^{-3}}$ (TC3) [23]. Composite TC3 (Fig. 1c) shows the most pronounced segregation morphology between Cu-rich,

CuZn-brass regions, and the Ti matrix. The presence of CuZn promotes melting at a lower temperature than Ti or Cu, resulting in the formation of large, bright clusters of brass phases. Compared with TC1 and TC2, the boundaries between the metallic phases are sharper, and rapid solidification during SPS minimizes intermetallic diffusion. The Al_2O_3 dispersion remains fine and uniform. The microstructure is most strongly segregated, which can lead to high local hardness in the CuZn regions and increased brittleness at the interfaces. [6] Raman spectroscopy (Figs. 2a–c) was employed to characterize the phase composition and the structural integrity of the graphene nanoplatelets reinforcement in three spark plasma sintered composites processed at 1000 °C, denoted TC1–TC3. In the low-wavenumber region below $\sim 800\,cm^{-1}$, the spectra of all three composites show several intense and relatively sharp bands, which can be associated with vibrational modes of Ti- and Al-containing oxides formed during SPS, in agreement with the presence of Al_2O_3 and Ti-based oxide species in the microstructure. For TC1, prominent peaks are observed in the 115–250 cm^{-1} interval, indicating a complex oxide/metal lattice response of the Ti-Cu-stainless steel-Al_2O_3 matrix. TC2 exhibits similarly strong bands in this range, but with an additional pronounced feature around $\sim 400\,cm^{-1}$, which can be tentatively linked to Mg-Al-O-related vibrations, consistent with the MgAl-containing matrix. The TC3 spectrum also shows a series of oxide-related bands clustered around 118–170 cm^{-1}, although with a lower absolute intensity, suggesting a somewhat different balance between metallic and oxide phases compared with TC1 and TC2. Overall, the intensity of the oxide-related bands is highest in TC2, indicating a particularly strong contribution of oxide phases to the Raman response of the MgAl-containing composite. Combining the oxide-related and carbon-related Raman features, a consistent picture emerges for the influence of matrix chemistry on GNP stability during SPS. TC2, which contains MgAl in place of stainless steel, exhibits the most intense oxide-related bands together with the lowest 2D/G ratio, indicating that the MgAl-modified matrix promotes extensive oxide formation and a more pronounced structural degradation or exfoliation of the GNPs. In contrast, TC1 shows a somewhat lower relative oxide intensity and the highest 2D band intensity, suggesting that the Ti-Cu-stainless steel-Al_2O_3 matrix is less detrimental to the graphitic stacking of the GNPs under the same sintering conditions. TC3 shows an intermediate Raman response, with oxide and carbon bands of comparable relative intensity and a 2D/G ratio between those of TC1 and TC2, indicating a balance between preserving and disordering the graphene structure. Overall, the Raman analysis of TC1–TC3 shows that SPS at 1000 °C yields composites in which the GNP reinforcement remains largely sp^2-hybridized but exhibits a substantial density of structural defects. At the same time, the matrix composition clearly affects the extent of GNP degradation and the formation of oxide phases. The stainless-steel-containing composite (TC1) shows the best retention of the graphitic 2D response, whereas the MgAl-containing composite (TC2) exhibits stronger oxide signatures and a more strongly perturbed graphene structure. These findings provide a microstructural basis for correlating the Raman response with the mechanical, thermal, and tribological behaviour of the SPS-processed Ti-Cu-based GNP-reinforced composites discussed in the following sections. These trends in the D/G and 2D/G intensity ratios are consistent with previous studies on graphene nanoplatelet-reinforced Ti-based composites consolidated by spark plasma sintering, in which Raman spectroscopy likewise revealed partial retention of multilayer GNPs, along with defect-induced D-band enhancement and carbide formation at the Ti-C interface [20].

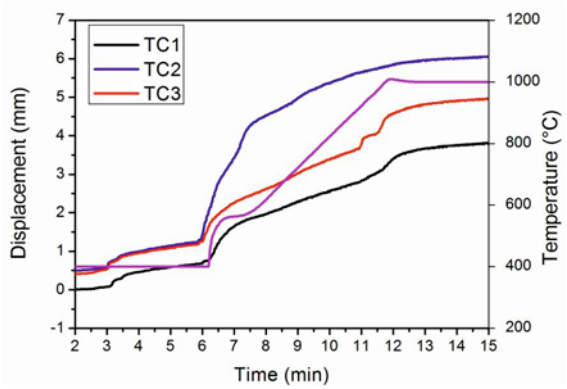

Fig. 3. Sintering curves (punch displacement) versus time together with the programmed SPS temperature profile for friction-composite samples TC1–TC3. Heating was 100 °C min^{-1} up to 1000 °C with a 10 min dwell.

3.2. Sintering behaviour

Figure 3 shows the sintering curves (punch displacement) for TC1–TC3 recorded during SPS at 1000 °C (10 min dwell, 100 °C min^{-1}). All compositions exhibit a latent stage with practically no displacement up to ~ 400 °C, followed by a rapid densification regime between ~ 600 and 950 °C. During the dwell, only minor additional displacement is detected, confirming completion of densification. The total displacement varies with composition: TC2 > TC3 > TC1, consistent with their distinct densification kinetics under identical SPS conditions. Final displacement is highest for TC2 (~ 6.0 mm), followed by TC3 (~ 5.0 mm) and TC1 (~ 3.7 mm).

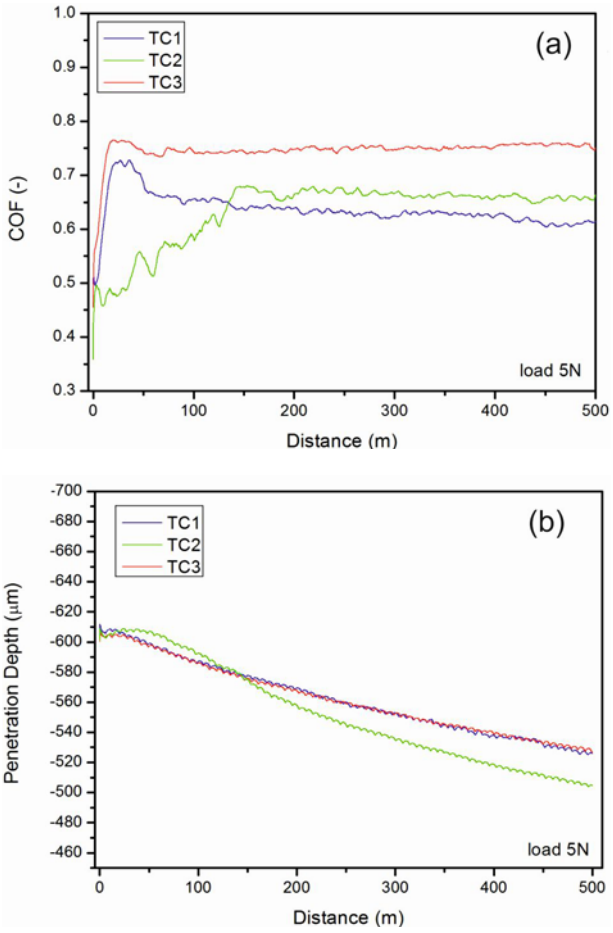

Fig. 4. (a) COF (–) vs. distance (m) and (b) penetration depth (μm) vs. distance (m).

3.3. Coefficient of friction at 350°C

In this work, COF was measured at 350 °C. Figure 4a shows the evolution of the coefficient of friction (COF) during 500 m of sliding under a normal load of 5 N. All composites underwent a short run-in phase, but with different dynamics. Composite TC1 exhibited a rapid increase of COF to ∼ 0.73, followed by a decrease to a stable level of ∼ 0.62 after approximately 50 m. Composite TC2 started with the lowest friction (∼ 0.36–0.40), but the COF gradually increased over time. Stabilisation occurred only after about 150 m, at ∼ 0.66, which indicates a progressive development of the load-bearing tribofilm. Composite TC3 achieved the shortest run-in phase and stabilised almost immediately at the highest, but very stable, value of ∼ 0.75 [17]. Figure 4b illustrates the change in penetration depth of the counter ball over time (sliding distance). All composite systems exhibited a monotonic increase in penetration from an initial depth. The largest value was achieved by composite TC2, reaching a final penetration depth of ∼ 100 μm, whereas TC1 and TC3 showed a very similar final shift of about ∼ 75 μm. This indicates surface strengthening and a greater ability to form a thicker, more continuous tribofilm in composites TC1 and TC3 [18]. Mean values of the coefficient of friction with standard deviations for each of the investigated composites are as follows: (i) TC1 0.636 ± 0.03, (ii) TC2 0.633 ± 0.058, and (iii) TC3 0.765 ± 0.023.

3.4. Wear mechanisms at 350°C

All SEM/EDS and confocal wear-track analyses in this section correspond to the hot tribological tests at 350 °C. The wear track of the friction composite 40Ti-25Cu-15SSt-15Al_2O_3-5GNPs (TC1), sintered by SPS (shown in Fig. 5a), consists of a system of long grooves in the sliding direction with numerous cracks and delaminated scales of the tribofilm. Locally, cavities formed by particle pull-out are visible. The morphology of the track indicates a combination of ploughing and delamination, together with an incoherent "flaky" oxide. The EDS map in Fig. 5d illustrates strong enrichment of Fe and Cr in vertical bands along with O, indicating the formation of Fe/Cr oxides originating from the austenitic component. Ti and O form secondary TiO_2 grains, while C is dispersed but not continuous. Cu appears in a mosaic-like distribution. The tribochemically formed film is non-compact, and the presence of hard Fe/Cr oxides and delaminating scales increases the fraction of abrasive-adhesive wear [19]. The surface of the composite 40Ti-25Cu-15MgAl-15Al_2O_3-5GNPs (TC2), shown in Fig. 5b, is more coated with continuous tribofilm areas. The grooves are shallower than in TC1, but large-scale delamination and locally extruded islands are observed. The dominant mechanism is oxidative sliding wear. The EDS map in Fig. 5e indicates that, in addition to Ti, Cu, Al, and O, Mg is distinctly present. Together with Al and O, it likely forms $MgAl_2O_4$ spinel, which appears in compact fields. Carbon (from GNPs) is distributed across the entire surface but with variable intensity. In TC2, a more stable and harder oxide-spinel layer forms, reducing groove depth; however, under local overload, these islands undergo brittle delamination. The wear track of the composite 40Ti-25Cu-15CuZn-15Al_2O_3-5GNPs (TC3), shown in Fig. 5c, is the smoothest, with large continuous areas of "glaze" film, minimal deep grooves, and only scattered microcracks. Sliding occurs predominantly over the compact tribofilm, with only a minor contribution from debris. The EDS map of the composite in Fig. 5f shows that Cu-rich regions predominate and overlap with O and C. This indicates the presence of a Cu-oxide/carbon film. Ti is present as a fine TiO_2 dispersion, while Fe/Cr are minor. The uniform distribution of carbon confirms the incorporation of GNPs into the lubricating tribofilm. A mixture of Cu- and Zn-oxides with carbon produces a compact, glaze-like Cu/Zn-oxide-

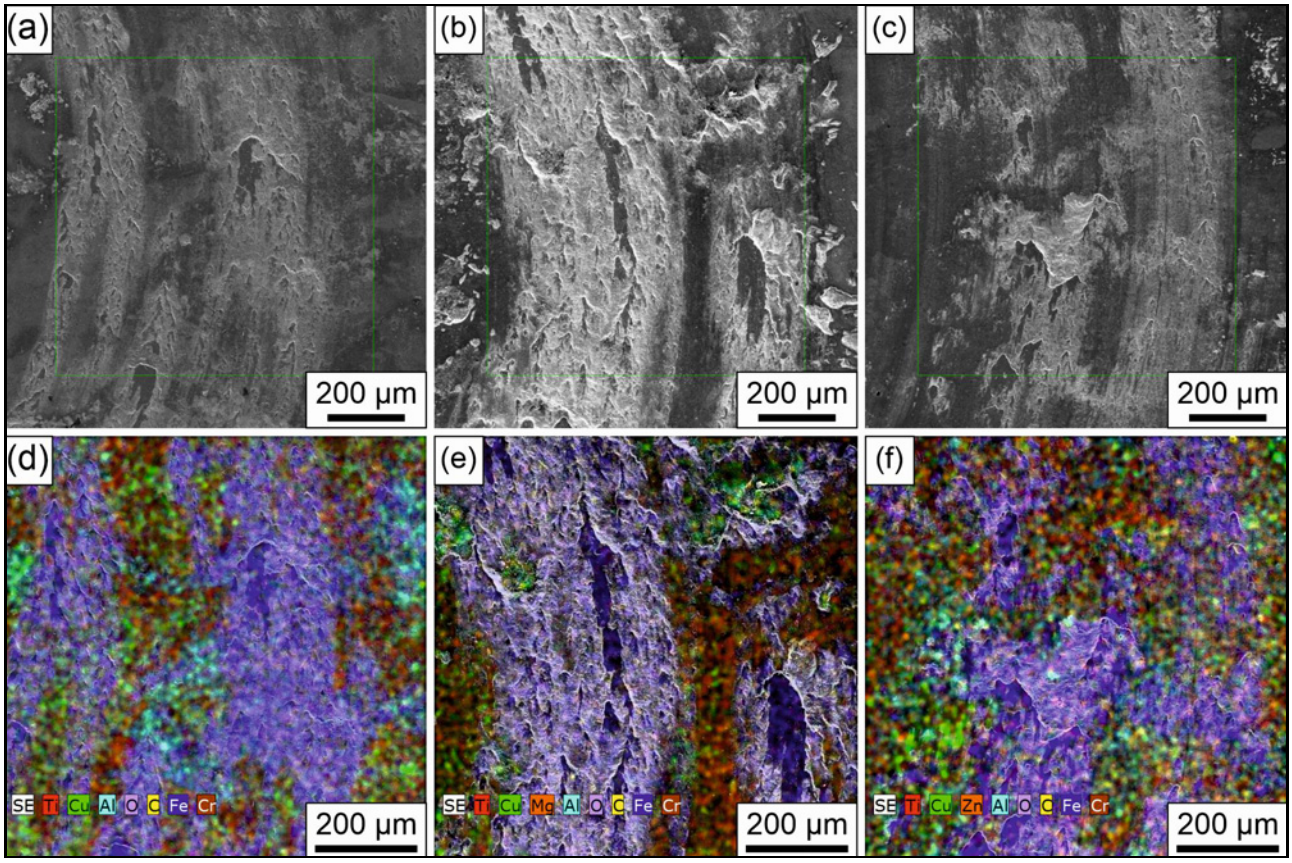

Fig. 5. SEM and EDS mapping of tribo tracks of samples (a), (d) TC1; (b), (e) TC2; and (c), (f) TC3.

-carbon tribofilm, as suggested by SEM/EDS and topographical evidence, in line with previous reports on Cu-based SPS friction materials [24, 25]. At 350 °C, the system transitions to a tribo-oxidative regime, and the composition of the metallic component determines the type and stability of the film. The stainless-steel addition (TC1) generates Fe/Cr oxides and delaminating scales, which increase the abrasive fraction of wear. The MgAl addition (TC2) promotes the formation of hard $MgAl_2O_4$ spinel, which protects against ploughing, but under local overload, it fractures and delaminates. The CuZn addition (TC3), together with Cu and GNPs, produces a continuous Cu/Zn-oxide-carbon glaze film with low shear resistance – the morphologically most favourable variant. The SEM/EDS correlation suggests that the combination of the soft Cu phase and GNPs is the most effective at 350 °C for stabilising a self-lubricating tribofilm and minimising debris-induced wear. The TC1 surface exhibits the roughest topography, with a wide, deep longitudinal groove and scattered cavities, indicating a heterogeneous, discontinuous tribofilm. TC2 exhibits a flatter track with a single, shallower depression and extended smooth plateaus, consistent with locally compact but brittle oxide-spinel islands. TC3 displays the smoothest and most uniform track, with multiple very shallow, low-amplitude grooves, indicating a compact, continuous, glaze-like tribofilm. These confocal observations, Figs. 6a–c, agree with the SEM/EDS morphology (Figs. 5a–f) and with the penetration depth trends (Fig. 4b), where TC3 forms the most coherent load-bearing film under identical conditions.

Table 2. Tribological and wear properties of the investigated materials

Experimental materials	COF mean ± SD	Wear rate × 10^{-6} ($mm^3\,m^{-1}N^{-1}$) mean ± SD
TC1	0.636 ± 0.03	3.16 ± 1.02
TC2	0.633 ± 0.058	7.63 ± 1.53
TC3	0.765 ± 0.023	20.00 ± 4.42

For each composite (TC1–TC3), we performed at least three independent tests under the same conditions (350 °C, 5 N, 500 m). In Table 2, we present tribological and wear properties, along with the standard deviation (SD), from at least three repetitions.

3.5. XRD analysis

X-ray diffraction (XRD) measurements were performed using a Philips X'Pert Pro diffractometer

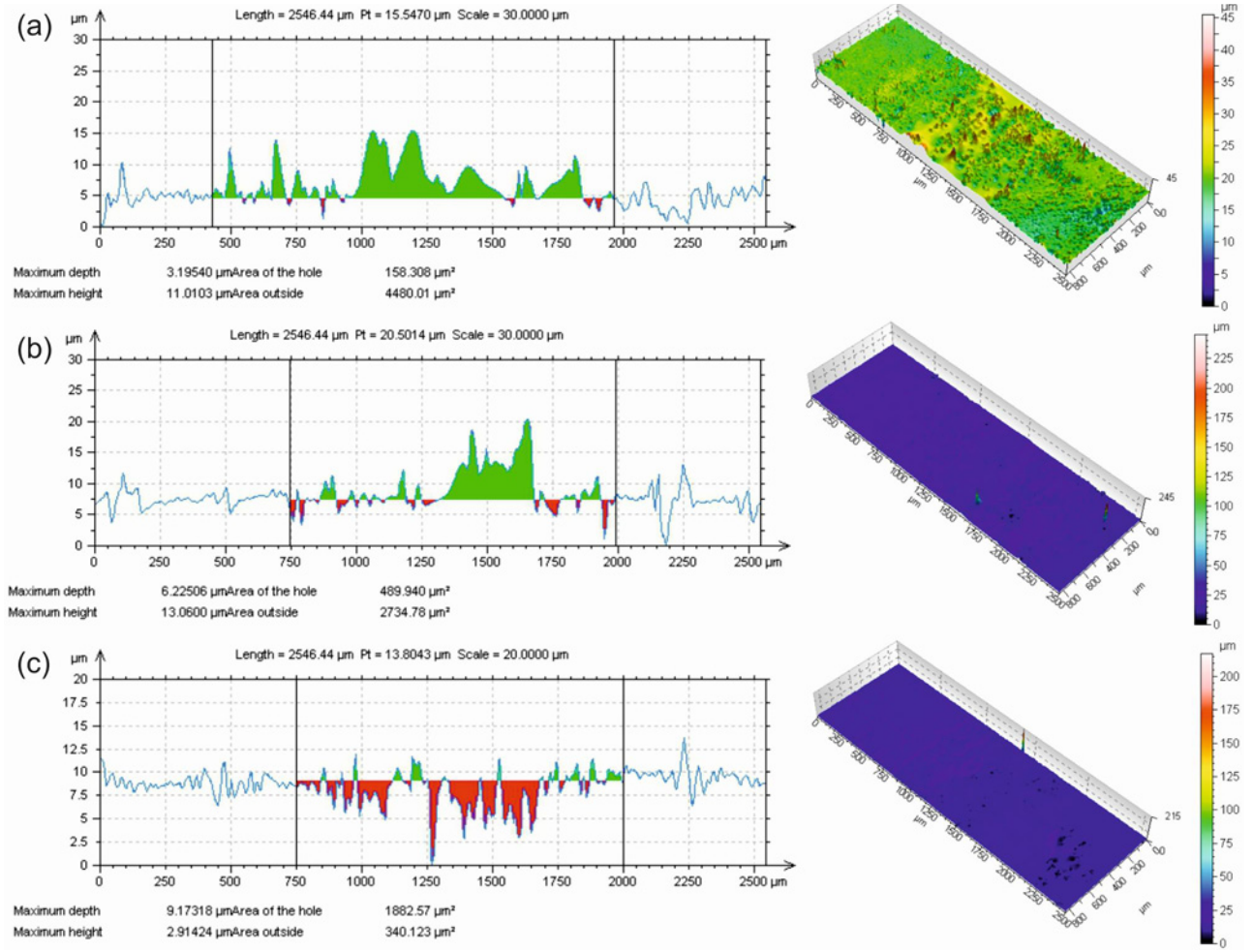

Fig. 6. Confocal 3D topography of the wear tracks with the corresponding line profiles after the tribological test at 350 °C and load 5 N: (a) TC1, (b) TC2, and (c) TC3.

(Malvern Panalytical, Almelo, The Netherlands) operating in Bragg-Brentano geometry with a Cu-Kα X-ray radiation source, Fig. 7. Data were collected in the 20°–100° 2θ range with a step size of 0.03° and a counting time of 30 s per step. Phase analysis was carried out using the *HighScore software package* (Malvern Panalytical, Almelo, The Netherlands) with the PDF-2 database. All TC1 to TC3 samples were measured before and after tribological testing (referred to as "no track" and "track," respectively). Each sample exhibited only minor changes in phase composition before and after testing. In all cases, no unambiguous phase transformation can be confirmed. This is likely because the tribological track is small relative to the total irradiated area, making it difficult to detect any newly formed phases. In the 45°–54° 2θ region, all samples show a relatively dense group of peaks corresponding to Cu-Ti intermetallic phases. Determining their exact stoichiometry is challenging or impossible; however, it is evident that more than one Cu-Ti phase is present in each sample. For evaluation, the following most probable phases were considered: Ti_3Cu_4 (tetragonal, I4/mmm), $TiCu_2$ (orthorhombic, Cmcm), CuTi (tetragonal, P4/nmm), and Cu_3Ti (orthorhombic, Cmc21), which were also synthesized in SPS, as described by [26]. All TC samples also contain hexagonal graphite. Notably, the TC3 sample without a tribological track shows a strong graphite reflection at 26.5° 2θ, which is most likely due to sample orientation; after tribological testing, this reflection becomes less pronounced. The Al_2O_3 phase (rhombohedral, R-3c) remains essentially unchanged, as does TiC (cubic, Fm3m), which is believed to have been formed during the SPS process [27]. The signals corresponding to stainless steel (Fe) in TC1, MgAl in TC2, and CuZn in TC3 also remain practically unchanged.

3.6. Wear mechanisms of counterparts

Analysis of the steel counterparts (100Cr6 steel balls) after tribological tests at 350 °C revealed only slight wear in all three systems, as shown in Figs. 8a–c. The wear scars were circular, with a diameter of

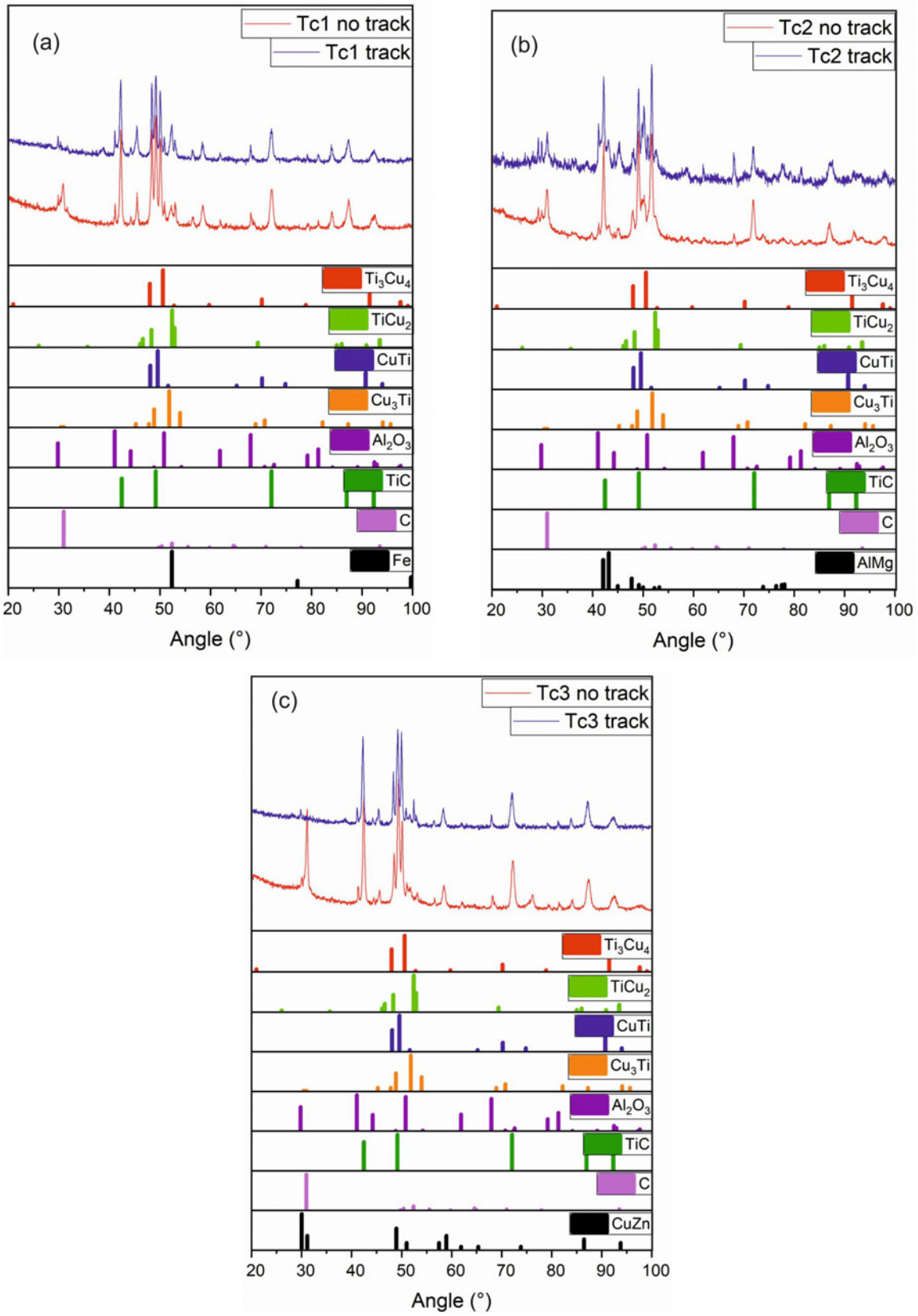

Fig. 7. Comparison of XRD from local spots in wear track and base material of samples: (a) TC1, (b) TC2, and (c) TC3.

approximately 1 mm, and showed fine parallel grooves aligned with the sliding direction, characteristic of a mild polishing wear mechanism. No evidence of severe damage, such as delamination, cavitation, or signifi-

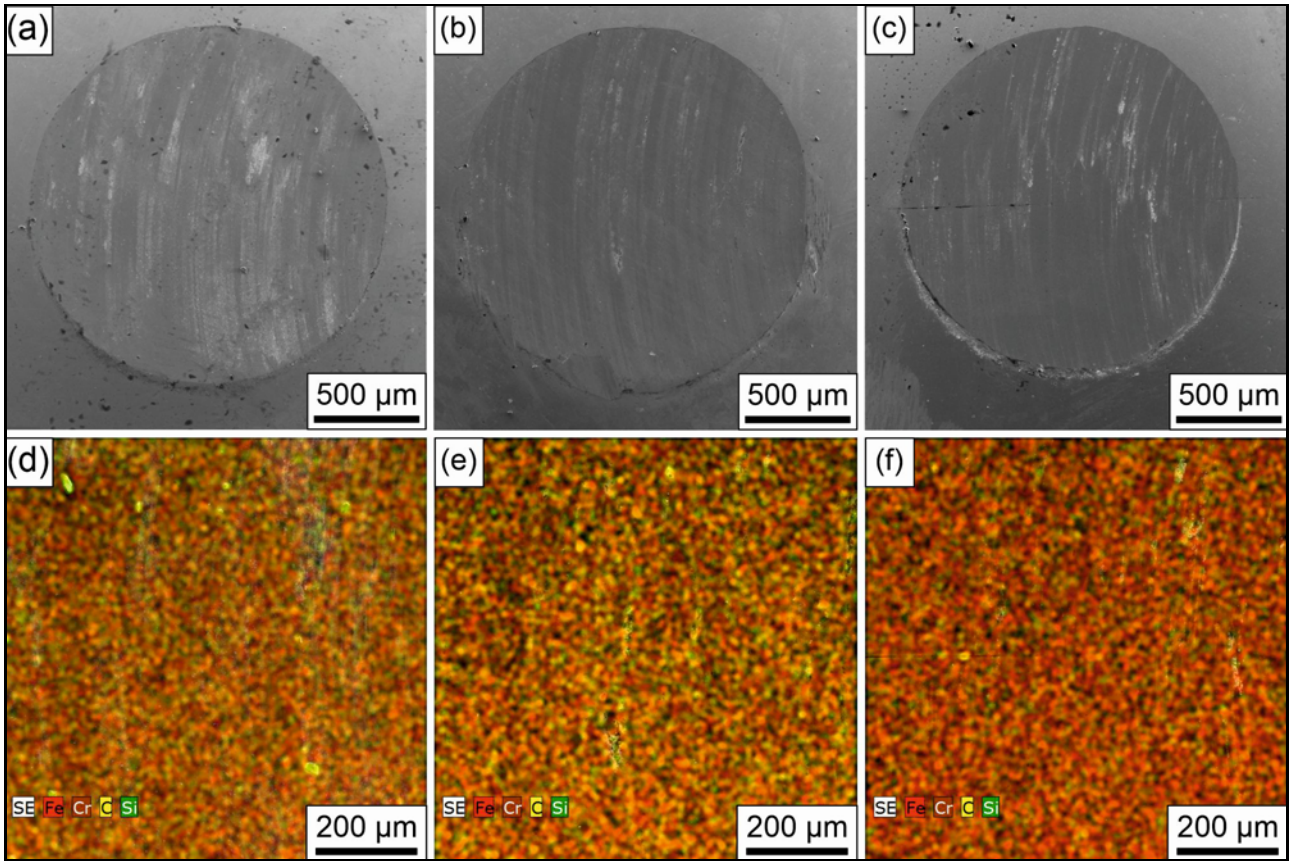

Fig. 8. SEM and EDS mapping of counterparts (100Cr6 steel balls) for samples (a), (d) TC1; (b), (e) TC2; and (c), (f) TC3 after hot tribological test.

cant material pile-up at the scar edges, was observed. Despite the overall mild wear, comparison of the scar topography revealed pronounced differences in surface smoothness. The smoothest, nearly mirror-like surface was observed on the counterbody tested against the TC3 composite. The counterbodies from the TC2 and TC1 systems exhibited progressively more pronounced micro-abrasion traces. In the case of TC3, a small amount of loose third-body particles was detected at the scar edges; however, they did not compromise the integrity of the central, smooth region. Elemental EDS analysis, Figs. 8d–f, confirmed these morphological observations and provided insight into the composition of the tribofilm. All three counterbodies were dominated by Fe and Cr signals originating from the steel substrate. A key finding was the presence of a weak but homogeneously distributed carbon signal across the entire wear scar area, most pronounced in the TC3 system. Importantly, no measurable transfer of elements (e.g., Ti, Cu, Al) from the composites to the counterbody surface was detected. These results indicate the formation of a stable tribofilm on the counterbody surface, effectively protecting it from extensive damage. This layer, consisting mainly of native steel oxides and a thin carbon film derived from GNPs, reduced direct metal-to-metal contact. At elevated temperatures, the formation of compact, smooth oxide-based layers, often referred to as “glaze layers”, is a key mechanism for achieving low friction and wear. Similar behaviour, namely, the formation of a continuous carbon film on steel and reduced counterbody wear, has also been reported in tribological tests of graphene-reinforced nanocomposites [27].

4. Conclusions

(1) All SPS-consolidated Ti-Cu-X-Al_2O_3-GNPs composites (X = stainless steel, MgAl, CuZn) form dense multiphase microstructures in which the metallic modifier controls phase segregation, porosity, and oxide formation. TC1 shows the highest microstructural heterogeneity, TC2 the most homogeneous metallic-phase distribution but higher porosity, and TC3 pronounced brass clusters with the lowest porosity and the most stable microstructure.

(2) Raman spectroscopy confirms that GNPs remain largely sp^2-hybridised after SPS at 1000 ℃, but with a high defect density. TC2 exhibits the strongest oxide-related bands and the lowest 2D/G ratio, indicating extensive oxide formation and a strongly perturbed graphene structure, whereas TC1 shows lower

relative oxide intensity and the strongest 2D band, corresponding to the best retention of graphitic stacking. TC3 displays an intermediate Raman response. These trends link matrix chemistry and GNP stability to the high-temperature tribological behaviour.

(3) Under dry sliding at 350 °C (5 N, 500 m, 100Cr6 steel ball), all composites reach a stable coefficient of friction between 0.62 and 0.77. TC1 and TC2 stabilise at ∼0.62 and ∼0.66 after run-in distances of ∼50 m and ∼150 m, respectively, while TC3 shows the shortest run-in and operates at the highest but very stable COF of ∼0.75. The corresponding mean COF values are 0.636 ± 0.030, 0.633 ± 0.058, and 0.765 ± 0.023 for TC1, TC2, and TC3, respectively.

(4) SEM/EDS and 3D profilometry reveal distinct tribofilms and wear mechanisms. TC1 is governed by a discontinuous Fe/Cr-oxide scale and pronounced abrasive-adhesive wear; TC2 forms shallower grooves and locally compact but brittle $MgAl_2O_4$-based islands; TC3 develops the smoothest wear track with extended, continuous glaze-like areas and a Cu/Zn-oxide-carbon tribofilm with homogeneous carbon distribution, providing the most coherent load-bearing surface.

(5) The wear rates of TC1, TC2, and TC3 are 3.16 ± 1.02, 7.63 ± 1.53, and 20.00 ± 4.42 × 10^6 mm^3 m^{-1} N^{-1}, respectively. Thus, TC3 combines the most stable high-temperature friction, the lowest penetration depth, and the mildest polishing wear of the 100Cr6 counterbodies, but exhibits a significantly higher wear rate than the composite itself. Overall, the Ti-Cu-CuZn-Al_2O_3-GNPs (TC3) composite offers the best compromise between friction stability and counterbody protection, whereas the stainless-steel- and MgAl-containing systems are preferable when minimising composite wear is prioritised, highlighting the need to tailor the waste-metal modifier to the intended functional requirements.

(6) Micro- and macro-diffraction analyses showed that no new phases were formed after the tribological tests. All samples show a relatively dense group of peaks corresponding to Cu-Ti intermetallic phases.

Acknowledgements

This research was supported by the Slovak Scientific Grant Agency within the framework of the projects VEGA 2/0113/23 and VEGA 2/0114/23.

References

[1] Ceramic vs. Semi Metallic Brake Pads, What's The Difference? Available online: https://www.bridgestonetire.com/learn/maintenance/ceramic-vs-metallic-brake-pads/#%CB%83 (accessed on 4 April 2021, ©2025 Bridgestone Americas Tire Operations, LLC)

[2] Introduction of powder metallurgy friction materials. Available online: https://www.chinagrtech.com/info/introduction-of-powder-metallurgy-friction-mat-90577681.html (accessed on 4 January 2024, ©Jiangsu Great Industrials Group Corp., Ltd All Rights Reserved)

[3] K. W. Liew, U. Nirmal, Frictional performance evaluation of newly designed brake pad materials, Mater. Design 48 (2013) 25–33. https://doi.org/10.1016/j.matdes.2012.07.055

[4] M. Podobova, V. Puchy, L. Falat, R. Dzunda, M. Besterci, Waste metals based metal-matrix ceramic-reinforced composites for friction applications, Kovove Mater. 60 (2022) 351–362. https://doi.org/10.31577/km.2022.6.351

[5] P. Zhang, L. Zhang, K. Fu, J. Cao, C. Shijia, X. Qu, Effects of different forms of Fe powder additives on the simulated braking performance of Cu-based friction materials for high-speed railway trains, Wear 414–415 (2018) 317–326. https://doi.org/10.1016/j.wear.2018.09.006

[6] Z. A. Munir, U. Anselmi-Tamburini, M. Ohyanagi, The effect of electric field and pressure on the synthesis and consolidation of materials: A review of spark plasma sintering, J. Mater. Sci. 41 (2006) 763–777. https://doi.org/10.1007/s10853-006-6555-2

[7] N. Xiao, K. Yang, X. Yin, F. Zhang, Y. Wu, H. Zhang, B. Xiong, Y. F. Zhu, M. Duan, C. Zhang, Analysis of mechanical properties and tribological optimization of Ti-16wt.%Ni alloys with MgAl-Al_2O_3-graphene microchannels, Wear 510–511 (2022) 204515. https://doi.org/10.1016/j.wear.2022.204515

[8] S. P. Dwivedi, S. Sharma, Development and characterization of Cu-Ni-Al_2O_3 surface composite developed by friction stir process technique, Mater. Today Commun. 37 (2023) 107399. https://doi.org/10.1016/j.mtcomm.2023.107399

[9] A. L. Rominiyi, M. B. Shongwe, S. O. Jeje, P. A. Olubambi, Microstructure, tribological and oxidation behaviour of spark plasma sintered Ti-Ni-xTiCN composites, J. Alloys Compd. 890 (2022) 161857. https://doi.org/10.1016/j.jallcom.2021.16185

[10] A. Saxena, S. P. Dwivedi, A. Kaushik, S. Sharma, Investigation on mechanical properties of ZTA + Cr_3C_2 + Ni reinforced EN31 steel-based composite material: Micromechanical finite-element analysis, Proc. Inst. Mech. Eng. Part E: J. Process Mech. Eng. 237 (2022) 1378–1393. https://doi.org/10.1177/09544089221113141

[11] M. Beder, T. Varol, S. B. Akçay, Impact of high Al_2O_3 content on the microstructure, mechanical properties, and wear behavior of Al-Cu-Mg/Al_2O_3 composites prepared by mechanical milling, Ceram. Int. 50 (2024) 38610–38631. https://doi.org/10.1016/j.ceramint.2024.07.230

[12] C. Kaikilarli, D. Uzunsoy, H. A. Yeprem, Role of process control agent in the production of Al_2O_3-reinforced titanium matrix composites, Ceram. Int. 50 (2024) 16452–16462. https://doi.org/10.1016/j.ceramint.2024.02.130

[13] M. Bahraminasab, S. Ghaffari, H. Eslami-Shahed, Al_2O_3-Ti functionally graded material prepared by spark plasma sintering for orthopaedic applications,

Journal of Mech. Behav. of Biomed. Mater. 72 (2017) 82–89. https://doi.org/10.1016/j.jmbbm.2017.04.024
[14] B. N. Sharath, C. V. Venkatesh, A. Afzal, M. A. A. Baig, A. P. Kumar, Study on effect of ceramics on dry sliding wear behaviour of Al-Cu-Mg based metal matrix composite at different temperature, Mater. Today Proc. 46 (2021) 8723–8733. https://doi.org/10.1016/J.MATPR.2021.04.034
[15] X. J. Shen, X. Q. Pei, Y. Liu, S. Y. Fu, Tribological performance of carbon nanotube-graphene oxide hybrid/epoxy composites, Compos. Part B-Eng 57 (2014) 120–125. https://doi.org/10.1016/j.compositesb.2013.09.050
[16] S. Ranjan, B. Mukherjee, A. Islam, K. A. Pandey, R. Gupta, A. K. Keshri, Microstructure, mechanical and high temperature tribological behaviour of graphene nanoplatelets reinforced plasma sprayed titanium nitride coating, J. Eur. Ceram. Soc. 40 (2020) 660–671. https://doi.org/10.1016/j.jeurceramsoc.2019.10.043
[17] E. Omrani, A. D. Moghadam, A. K. Kasar, P. Rohatgi, P. L. Menezes, Tribological performance of graphite nanoplatelets reinforced Al and Al/Al_2O_3 self-lubricating composites, Materials 14 (2021) 1183. https://doi.org/10.3390/ma14051183
[18] A. Patil, G. Walunj, F. Ozdemir, R. K. Gupta, T. Borkar, Tribological behavior of carbon-based nanomaterial-reinforced nickel metal matrix composites, Materials 14 (2021) 3536. https://doi.org/10.3390/ma14133536
[19] W. Zhai, S. Narasimalu, L. B. Kong, K. Zhou, Carbon nanomaterials in tribology, Carbon 119 (2017) 150–171. https://doi.org/10.1016/j.carbon.2017.04.027
[20] W. Wang, H. Zhou, Q. Wang, B. Wei, S. Xin, Y. Gao, Microstructural evolution and mechanical properties of graphene-reinforced Ti-6Al-4V composites synthesized via spark plasma sintering, Metals 10 (2020) 737. https://doi.org/10.3390/met10060737
[21] Y. Ma, Y. Liu, S. Ma, H. Wang, Z. Gao, J. Sun, J. Tong, L. Guo, Friction and wear properties of dumbbell-shaped jute fiber-reinforced friction materials, J. Appl. Polym. Sci. 131 (2014) 40748. https://doi.org/10.1002/app.40748
[22] Y. Liu, Y. Ma, X. Lv, J. Yu, J. Zhuang, J. Tong, Mineral fibre reinforced friction composites: Effect of rockwool fibre on mechanical and tribological behavior, Mater. Res. Express 5 (2018) 095308. https://doi.org/10.1088/2053-1591/aad767
[23] M. Podobová, V. Puchý, R. Sedlák, D. Medved', R. Džunda, F. Kromka, Wear behaviour of graphene-reinforced Ti-Cu waste-metal friction composites fabricated with spark plasma sintering, Crystals 14 (2024) 948. https://doi.org/10.3390/cryst14110948
[24] M. Pellizzari, G. Cipolloni, Tribological behaviour of Cu based materials produced by mechanical milling/alloying and spark plasma sintering, Wear 376–377 B (2017) 958–967. https://doi.org/10.1016/j.wear.2016.11.050
[25] D. Berman, A. Erdemir, A. V. Sumant, Graphene: a new emerging lubricant, Mater. Today 17 (2014) 31–42. https://doi.org/10.1016/j.mattod.2013.12.003
[26] O. O. Shichalin, V. N. Sakhnevich, I. Y. Buravlev, A. O. Lembikov, A. A. Buravleva, S. A. Azon, S. B. Yarusova, S. N. Danilova, A. N. Fedorets, A. A. Belov, E. K. Papynov, Synthesis of Ti-Cu multiphase alloy by spark plasma sintering: Mechanical and corrosion properties, Metals 12 (2022) 1089. https://doi.org/10.3390/met12071089
[27] G. Sun, S. Zhuang, D. Jia, X. Pan, Y. Sun, F. Tu, M. Lu, Facile fabricating titanium/graphene composite with enhanced conductivity, Mater. Lett. 333 (2023) 133680. https://doi.org/10.1016/j.matlet.2022.133680